

Delaunay–Rips filtration: a study and an algorithm

Mattéo Clémot^{1*}, Julie Digne^{1,2} and Julien Tierny^{2,3}

¹LIRIS, Université Claude Bernard Lyon 1.

²CNRS.

³LIP6, Sorbonne University.

*Corresponding author(s). E-mail(s): matteo.clemot@univ-lyon1.fr;

Contributing authors: julie.digne@cnrs.fr;

julien.tierny@sorbonne-universite.fr;

Abstract

The Delaunay–Rips filtration is a lighter and faster alternative to the well-known Rips filtration for low-dimensional Euclidean point clouds. Despite these advantages, it has seldom been studied. In this paper, we aim to bridge this gap by providing a thorough theoretical and empirical analysis of this construction. From a theoretical perspective, we show how the persistence diagrams associated with the Delaunay–Rips filtration approximate those obtained with the Rips filtration. Additionally, we describe the instabilities of the Delaunay–Rips persistence diagrams when the input point cloud is perturbed. Finally, we introduce an algorithm that computes persistence diagrams of Delaunay–Rips filtrations in any dimension. We show that our method is faster and has a lower memory footprint than traditional approaches in low dimensions. Our C++ implementation, which comes with Python bindings, is available at <https://github.com/MClemot/GeoPH>.

Keywords: Persistent homology, algorithmic geometry, topological data analysis.

1 Introduction

Topological data analysis (TDA) provides various tools to handle topological properties of datasets. In particular, it allows to perform *topological inference* of point clouds, i.e., finding whether they feature interesting topological structures like connected components, cycles, or cavities, and have a measure of their *significance*. To do so, TDA relies on *filtrations*, which are increasing sequences of simplicial complexes over a set

of points. One of them, the (Vietoris)–Rips filtration, is a particularly versatile tool, as it can be applied in any metric space, and in particular in any Euclidean space \mathbb{R}^d . Unfortunately, the Rips filtration becomes prohibitively large as the number n of points increases, since the total number of simplices to consider is $2^n - 1$. Even its k -skeleton, i.e., the set of simplices with dimension at most k , has $\mathcal{O}(n^{k+1})$ simplices. Therefore, despite the availability of optimized implementations [1] – including parallelization on the CPU [2] or the GPU [3] – using the Rips filtration can be very computationally expensive, both in time and memory.

In low dimensional Euclidean spaces, one can leverage the Delaunay complex in order to build filtrations with a drastically reduced number of simplices. This is the case of the well-known α -filtration (i.e., the filtrations of α -complexes, originally introduced in [4]), also known as the Delaunay filtration [5]. It has the nice property to be topologically equivalent to the less combinatorial offset filtration, i.e., the filtration of the union of the increasing balls centered in the input points. On the contrary, the Rips filtration only provides an approximation of this offset filtration.

A less common way of constructing a filtration is to restrict the Rips filtration to the Delaunay complex, which we call here the *Delaunay–Rips filtration*, but which is also known as the *weak α -filtration*. It has been recently used for constructing a differentiable topological layer, for instance to incorporate topological priors in learning processes [6]. It was also compared to α -filtrations and Rips filtrations in classification tasks where it performed similarly in terms of accuracy [7]. In addition, while the Delaunay–Rips filtration, like the Rips filtration and contrary to the α -filtration, does not benefit from the topological equivalence to the offset filtration, it is faster to compute than the α -filtration since it relies on simplex diameters instead of (empty) minimum enclosing ball radii, which are more intensive to compute. Furthermore, its flag complex structure can be leveraged when computing its persistent homology.

To our knowledge, the Delaunay–Rips filtration and its persistent homology have seldom been studied and very few practical implementations are available (giotto-tda [8] proposes an implementation based on Ripser [1]). In this paper, we aim to study the Delaunay–Rips filtration and introduce a dedicated algorithm for computing its persistent homology. More precisely, we make the following contributions:

1. a theoretical and empirical study of the instabilities of Delaunay–Rips persistence diagrams and their distance to Rips persistence diagrams ([Sec. 4](#));
2. a dedicated algorithm to compute Delaunay–Rips persistence diagrams in any dimension ([Sec. 5](#));
3. a C++ implementation (with Python bindings) of this algorithm¹.

2 Related work

Much work has been done to improve the use of the Rips filtration. Algorithmically, it is common to compute cohomology instead of homology, which produces the same persistence diagrams. Ripser [1] specializes to Rips filtrations by representing implicitly the coboundary matrix and by dealing efficiently with the so-called *apparent* and *emergent pairs*. Concerning parallelism, the Rips filtration construction and the finding

¹available at this repository: <https://github.com/MClemot/GeoPH>

of the apparent pairs have been implemented on the GPU by Ripser++ [3], but not the matrix reduction step. A parallel implementation of this step on the CPU was proposed by giotto-ph [2], following the lockfree shared-memory approach of [9]. However, even with these parallel approaches, and even with a limitation on the dimension of the simplices and their value of the filtration, Rips and Čech filtrations remain large and become prohibitively costly to compute as the number n of points increases.

Reducing the size of filtrations

Linear-size filtrations depending on an approximating factor ε have been proposed to provide $(1 + \mathcal{O}(\varepsilon))$ -approximations of the Rips or the Čech filtrations [10–12]. Another way to reduce flag filtrations (that are made of flag complexes, like the Rips complexes) is to use *edge collapses* [13, 14] that return a smaller filtration with the same persistence homology, thereby speeding up its computation. Finally, other methods select a reduced set of landmarks to build smaller filtrations that also provide a nice estimation of the topology [15, 16].

Learning-based approaches

Another way to avoid the expensive computation of persistent diagrams of the Rips filtration consists in using a neural network that was previously trained to map point sets to some vectorization of these diagrams. For instance, TopologyNet [17] and RipsNet [18] propose architectures (based respectively on the EdgeConv [19] and DeepSets [20] architectures) that can learn finite-dimensional embeddings of Rips persistence diagrams.

Persistent homology in Euclidean spaces

Some optimizations are possible when considering point clouds in Euclidean spaces (all the more so in low dimension). In particular, the *reduced* Vietoris–Rips filtration [21] has the same 1-dimensional persistent homology (PH^1) than the Rips filtration but contains only $\mathcal{O}(n^2)$ instead of $\mathcal{O}(n^3)$ triangles, relying on the relative neighborhood graph (see Sec. 3.5). This enables a faster and more memory-efficient computation of the PH^1 of the Rips filtration of low-dimensional points clouds. In the Euclidean plane, minmax length triangulations can be leveraged to further speed up the search for triangles that destroy a PH^1 class [22]. Besides, working in a low-dimensional Euclidean space allows leveraging Delaunay complexes to build filtrations (e.g., Delaunay and Delaunay–Rips filtrations) with a drastically reduced number of simplices, while still providing a good approximation of the offset filtration. These Delaunay complexes have also been used in the context of bifiltrations [23–25], which are beyond the scope of this work.

Applications

The Delaunay–Rips filtration was used for shape classification (based on random forests) or biophysical time series classification (based on SVMs) [7]. The authors claim that, in practice, the instability of the Delaunay–Rips persistence diagrams (see Sec. 3.4) have little impact on the accuracy of these applications (in comparison to

using the Rips- or the α -filtration). The Delaunay–Rips filtration was also successfully used to build topological loss functions that enable regularizing or incorporating topological priors in machine learning models [6].

3 Background

We consider a point cloud X with n points in the d -dimensional Euclidean space \mathbb{R}^d . An *abstract simplicial complex* is a collection \mathcal{K} of subsets $\sigma \subset X$ (called *simplices*) that is closed under taking subsets (called their *faces*), i.e., if $\sigma \in \mathcal{K}$ and $\tau \subset \sigma$, then $\tau \in \mathcal{K}$. We write $\mathcal{K}^k = \{\sigma \in \mathcal{K} \mid \dim \sigma = k\}$ the set of k -dimensional simplices of \mathcal{K} , and $\mathcal{K}^{(k)} = \{\sigma \in \mathcal{K} \mid \dim \sigma \leq k\}$ its k -skeleton. We also denote $\Delta(X) = 2^X \setminus \{\emptyset\}$ the full abstract simplicial complex spanned by X .

Another simplicial complex of interest is the Delaunay complex $\text{DEL}(X)$. To be properly defined, it requires that no $d+1$ points lie on the same hyperplane and that no $d+2$ points lie on the same $(d-1)$ -dimensional sphere, which we refer to as the general position hypothesis. The non-general positions indeed induces combinatorial changes (e.g., edge flips) in the Delaunay complex, leading to instabilities in the Delaunay–Rips persistence (see Sec. 3.4). In the worst case, the Delaunay complex contains $\mathcal{O}(n^{\lceil d/2 \rceil})$ simplices [26]. In practice however, one can expect a construction time complexity in $\mathcal{O}(n \log n)$, with a constant exponential in the ambient dimension d for uniform random vertices, thanks to a pre-sorting [27, 28].

We use in the following homology groups and persistent homology groups. We refer the reader to reference books [29, 30] for a complete introduction to simplicial and persistent homology.

3.1 Persistence diagrams and bottleneck distance

For a given dimension $k \geq 0$, the k -dimensional *persistence diagram* $\text{dgm}^k(\mathcal{F})$ of a filtration \mathcal{F} is a multiset of points $(b, d) \in \mathbb{R}^2$ where b and d are respectively the *birth* and the *death* of a k -dimensional persistence class. Persistence diagrams can be compared with metrics borrowed from optimal transport, namely the Wasserstein and bottleneck distances. Given D and D' two persistence diagrams corresponding to the same persistent homology dimension, we define their *augmented* diagrams $\overline{D} = D \cup \Pi(D')$ and $\overline{D}' = D' \cup \Pi(D)$ where Π is the map on \mathbb{R}^2 that projects orthogonally on the diagonal, i.e., $\Pi : (b, d) \mapsto (\frac{b+d}{2}, \frac{b+d}{2})$. The set of bijections between the two is noted $\Psi = \text{Bij}(\overline{D}, \overline{D}')$. Then the cost c_∞ between two points $x \in \overline{D}$ and $y \in \overline{D}'$ is defined as 0 if both points belong to the diagonal and $\|x - y\|_\infty$ otherwise. This permits to define the bottleneck distance

$$d_b(D, D') = \min_{\psi \in \Psi} \max_{x \in \overline{D}} c_\infty(x, \psi(x)). \quad (1)$$

3.2 Persistence modules and interleavings

Let $\mathcal{F} = (\mathcal{F}_r)_{r \geq 0}$ be a filtration. For all $r \leq r'$, the inclusion map $\iota_{r,r'} : \mathcal{F}_r \hookrightarrow \mathcal{F}_{r'}$ induces, when applying the homology functor, a homomorphism $(\iota_{r,r'})_* : H^k(\mathcal{F}_r) \hookrightarrow$

$H^k(\mathcal{F}_{r'})$. This allows to define the k -th *persistence module* of \mathcal{F} , which is defined as the collection $(H^k(\mathcal{F}_r))_{r \geq 0}$ with these induced inclusions maps $((\iota_{r,r'})_*)_0 \leq r \leq r'$.

Two persistence modules $\mathbb{V} = (V_r)_{r \geq 0}$ and $\mathbb{W} = (W_r)_{r \geq 0}$ are said to be strongly ε -interleaved if there exist homomorphisms $\Phi_r : V_r \rightarrow W_{r+\varepsilon}$ and $\Psi_r : W_r \rightarrow V_{r+\varepsilon}$ for all $r \geq 0$, such that the following diagrams commute for all $r \leq r'$ (where horizontal maps are the induced inclusions) [31]:

$$\begin{array}{ccc}
\begin{array}{ccc}
V_{r-\varepsilon} & \xleftarrow{\quad} & V_{r+\varepsilon} \\
\Phi_{r-\varepsilon} \searrow & & \nearrow \Psi_r \\
& W_r &
\end{array} & \quad &
\begin{array}{ccc}
V_{r+\varepsilon} & \xleftarrow{\quad} & V_{r'+\varepsilon} \\
\Psi_r \nearrow & & \nearrow \Psi_{r'} \\
W_r & \xrightarrow{\quad} & W_{r'}
\end{array} \\
& & (2) \\
\begin{array}{ccc}
& V_r & \\
\Psi_{r-\varepsilon} \nearrow & \searrow \Phi_r & \\
W_{r-\varepsilon} & \xleftarrow{\quad} & W_{r+\varepsilon}
\end{array} & \quad &
\begin{array}{ccc}
V_r & \xleftarrow{\quad} & V_{r'} \\
\Phi_r \searrow & & \nearrow \Phi_{r'} \\
W_r & \xleftarrow{\quad} & W_{r'+\varepsilon}
\end{array}
\end{array}$$

The strong stability theorem [32] states that if two persistence modules \mathbb{V} and \mathbb{W} are strongly ε -interleaved, then:

$$d_b(dgm(\mathbb{V}), dgm(\mathbb{W})) \leq \varepsilon.$$

The multiplicative version of interleaving (see e.g., [10]) is also of interest. In this case, we instead have homomorphisms $\Phi_r : V_r \rightarrow W_{r\eta}$ and $\Psi_r : W_r \rightarrow V_{r\eta}$ and the corresponding commutative diagrams. By reparameterizing the filtrations on a log-scale, the strong stability theorem becomes in its multiplicative version that if two persistence modules are multiplicatively strongly η -interleaved, then:

$$d_b(\log dgm(\mathbb{V}), \log dgm(\mathbb{W})) \leq \log(\eta) \text{ with } \log D = \{(\log b, \log d) \mid (b, d) \in D\}.$$

3.3 Filtrations for point clouds

The *offset filtration* $(\mathcal{O}_r(X))_{r \geq 0}$, where $\mathcal{O}_r(X) = \bigcup_{x \in X} B_r(x)$ is the union of the closed balls of radius r centered in the vertices in X , provides a multi-scale representation of X which is of theoretical interest in topological data analysis (see Fig. 1, top). However, the offset filtration is hard to use directly because of its non-combinatorial nature. One may rather use the *nerves* of this set of closed balls (hereafter noted the *nrv* operator), known as the *Čech filtration* $(\check{\mathcal{C}}_r(X))_{r \geq 0}$, where

$$\check{\mathcal{C}}_r(X) = \left\{ \sigma \subset X \mid \bigcap_{x \in \sigma} B_r(x) \neq \emptyset \right\} = \text{nrv}\left(\left(B_r(x)\right)_{x \in X}\right). \quad (3)$$

By the nerve theorem [33], the two filtrations are topologically equivalent, i.e., for each $r \geq 0$, $\mathcal{O}_r(X)$ and $\check{\mathcal{C}}_r(X)$ are homotopy equivalent and therefore have isomorphic homology groups. The scale at which a simplex $\sigma \subset X$ is introduced in the Čech filtration is the radius of the minimum enclosing ball of σ , noted *meb*(σ), so that we can also write $\check{\mathcal{C}}_r(X) = \{\sigma \subset X \mid \text{meb}(\sigma) \leq r\}$. A common approximation consists

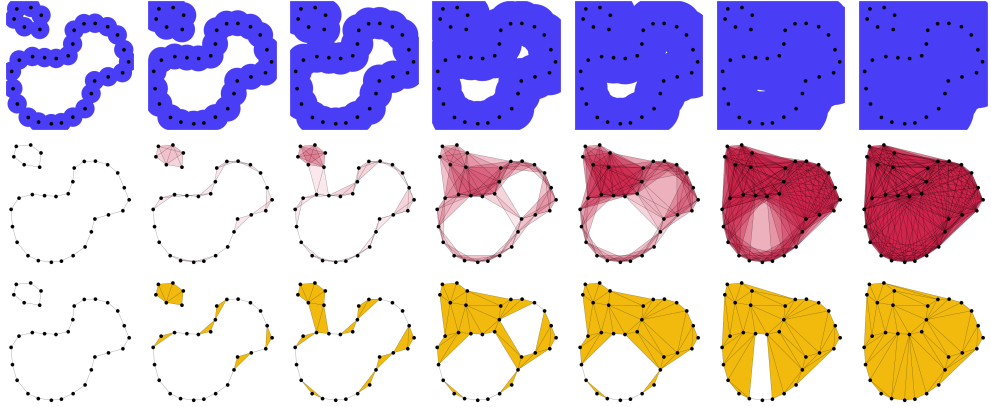


Fig. 1 Offset filtration (top), Rips filtration (middle) and Delaunay–Rips filtration (bottom) for the same point cloud in \mathbb{R}^2 . Notice that in the second to last column, the Rips and Delaunay–Rips simplicial complexes – for the same diameter value – do not feature the same number of topological handles.

in replacing this value by the diameter $\delta(\sigma) = \max_{x,y \in \sigma} \|x - y\|_2$. This leads to the well-studied *Rips filtration* $(\mathcal{R}_r(X))_{r \geq 0}$, where²:

$$\mathcal{R}_r(X) = \{\sigma \subset X \mid \delta(\sigma) \leq 2r\}. \quad (4)$$

Jung’s theorem [34] establishes that for any simplex σ , $\delta(\sigma) \leq 2 \text{meb}(\sigma) \leq \sqrt{2}\delta(\sigma)$. Therefore, we always have the inclusions $\check{\mathcal{C}}_r(X) \subseteq \mathcal{R}_r(X) \subseteq \check{\mathcal{C}}_{\sqrt{2}r}(X)$ which make the persistence modules of the Rips and Čech filtrations multiplicatively, strongly $\sqrt{2}$ -interleaved (using as Φ_r and Ψ_r the homomorphisms induced by the inclusion maps $\check{\mathcal{C}}_r(X) \hookrightarrow \mathcal{R}_r(X)$ and $\mathcal{R}_r(X) \hookrightarrow \check{\mathcal{C}}_{\sqrt{2}r}(X)$). Hence, in the general case, with the strong stability theorem, $d_b(\log \text{dgm}_{\mathcal{R}}(X), \log \text{dgm}_{\check{\mathcal{C}}}(X)) \leq \log \sqrt{2}$.

Delaunay-restrained filtrations

Both Čech and Rips filtrations consider in total $2^n - 1$ simplices, or $\mathcal{O}(n^{k+1})$ simplices if the dimension of those simplices is bounded up to k (e.g., if we are only interested in the first $(k-1)$ -dimensional persistent homologies). For low-dimensional data, it is possible to leverage the Delaunay complex in order to reduce the number of considered simplices and therefore make the computations far more scalable, for a fixed dimension. In particular, one can consider intersection of the Čech complex with the Delaunay complex of X , known as the *Delaunay–Čech filtration* $(\mathcal{D}\check{\mathcal{C}}_r(X))_{r \geq 0}$:

$$\mathcal{D}\check{\mathcal{C}}_r(X) = \left\{ \sigma \in \text{DEL}(X) \mid \bigcap_{x \in \sigma} B_r(x) \neq \emptyset \right\} = \text{nrv}\left(\left(B_r(x)\right)_{x \in X}\right) \cap \text{DEL}(X). \quad (5)$$

²Rips complexes are often formulated as $\mathcal{R}_r(X) = \{\sigma \subset X \mid \delta(\sigma) \leq r\}$ (i.e., diameter bounded by r), but we double here the threshold value to match the scale of Čech filtrations (i.e., radius bounded by r).

This one is slightly distinct from the commoner *Delaunay filtration*, also called the α -filtration³. However, the Čech, Delaunay–Čech and Delaunay filtrations are known to be topologically equivalent in the sense that they have isomorphic persistent homology [5]. More precisely, for any r , there exists a sequence of elementary collapses that transforms $\check{\mathcal{C}}_r(X)$ into $\mathcal{D}\check{\mathcal{C}}_r(X)$. Eventually, we can also define the *Delaunay–Rips filtration* $(\mathcal{DR}_r(X))_{r \geq 0}$ [7], sometimes referred as the *weak α -filtration* [8], as the intersection of the Rips filtration with the Delaunay complex (see Fig. 1, bottom):

$$\mathcal{DR}_r(X) = \{\sigma \in \text{DEL}(X) \mid \delta(\sigma) \leq 2r\}. \quad (6)$$

In addition to featuring less simplices because restrained to $\text{DEL}(X)$, this is also faster to compute than the Delaunay–Čech filtration, as the computation of each simplex's minimum enclosing ball is not required. However, Rips and Delaunay–Rips filtrations are not topologically equivalent (see Fig. 1). In addition, the computational cost of the Delaunay triangulation scales exponentially with the ambient dimension d and therefore becomes prohibitively high when d increases. Consequently, the use of this filter is only conceivable for low-dimensional data (up to the order of 10).

In the following, given a filtration $(\mathcal{F}_r(X))_{r \geq 0}$, we write $\text{dgm}_{\mathcal{F}}^k(X)$ the associated k -dimensional persistence diagram. We will omit X when the considered point cloud is not ambiguous.

3.4 (In)stability of point cloud persistence

Persistence diagrams – for some filtrations – are known to be stable to perturbations of the input. In particular, the bottleneck distance between the persistence diagrams of either Rips or Čech filtration of X and Y is upper bounded by their Gromov–Hausdorff distance [35, 36]:

$$d_b(\text{dgm}_{\mathcal{R}}(X), \text{dgm}_{\mathcal{R}}(Y)) \leq 2 d_{\text{GH}}(X, Y) \quad (7)$$

$$d_b(\text{dgm}_{\check{\mathcal{C}}}(X), \text{dgm}_{\check{\mathcal{C}}}(Y)) \leq 2 d_{\text{GH}}(X, Y) \quad (8)$$

Similar stability results exist for comparing the L_p -Wasserstein distances \mathcal{W}_p and the p -norm of the perturbations, when $p < \infty$ [37].

On the contrary, persistence diagrams for the Delaunay–Rips filtration may feature instabilities [7] in the non-general positions for the Delaunay complex. See Fig. 2 for an example of such instability in the plane. Nonetheless, those instabilities can be characterized (see Sec. 4).

3.5 Geometric structures

In this section, we introduce some geometric or combinatorial objects and their links with persistent homology.

³defined as the nerve of the Voronoi balls, i.e., $\mathcal{D}_r(X) = \{\sigma \subset X \mid \bigcap_{x \in \sigma} \text{Vor}_r(x, X) \neq \emptyset\}$ where $\text{Vor}_r(x, X) = B_r(x) \cap \text{Vor}(x, X)$. The scale at which a simplex appears in this filtration is the minimum radius of an empty circumsphere of σ , which can be greater than $\text{meb}(\sigma)$.

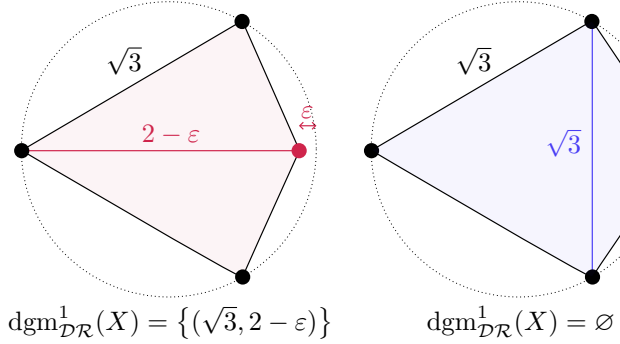


Fig. 2 Illustration of the instability of persistence diagrams for the Delaunay–Rips filtration. Left: the red point is slightly inside the black unit circle and there exists one positive persistent pair, killed by the red edge. Right: the blue point is slightly outside the unit circle. The blue edge is therefore a Delaunay edge, hence the two triangles appear at the same value $\sqrt{3}$ as the black cycle.

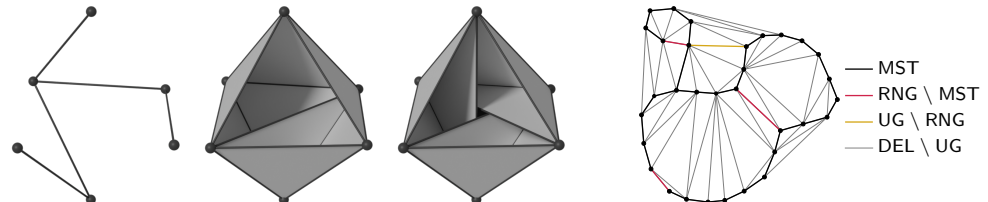


Fig. 3 **Left:** $\text{MST}(X)$ (left), $\text{MSA}^2(\text{DEL}(X))$ (center) and $\text{MSA}^2(\Delta(X))$ (right) of the same points $X \subset \mathbb{R}^3$. For the two MSA^2 s, there is no remaining 1-cycle that is unfilled by the triangles (i.e., it is 2-spanning), yet no cavity is created (i.e., it is 2-acyclic). **Right:** illustration of the inclusions $\text{MST}(X) \subset \text{RNG}(X) \subset \text{UG}(X) \subset \text{DEL}(X)$ on a planar point cloud $X \subset \mathbb{R}^2$.

Minimum spanning acycles

Minimum spanning acycles, originally introduced in [38], are a proposed generalization of minimum spanning trees. Let \mathcal{K} be a simplicial complex and $S \subset \mathcal{K}^k$ a set of k -simplices. We say that S is a k -acycle if, informally, S does not enclose any k -dimensional hole. This corresponds to $\beta_k(\mathcal{K}^{(k-1)} \cup S) = 0$. We say that S is k -spanning if S fills all the $(k-1)$ -dimensional holes formed by all the $(k-1)$ -simplices. This corresponds to $\beta_{k-1}(\mathcal{K}^{(k-1)} \cup S) = 0$. Finally, S is said to be a k -spanning acycle if it has both properties. The definition of a spanning tree corresponds to that of a 1-spanning acycle: a set of edges E such that $\beta_0(X \cup E) = 0$ (spanning-ness: each vertex is reached by the set of edges) and $\beta_1(X \cup E) = 0$ (acyclicity).

Given a weight function $w : \mathcal{K}^k \rightarrow \mathbb{R}$, a minimum k -spanning acycle is a k -spanning acycle which minimizes the total weight of its simplices. When w is injective, we have a total ordering on the k -faces and the minimum k -spanning acycle is unique ([39], Lemma 3.8). When it is not (e.g., when w is the diameter δ), we only have a partial ordering, that however can be extended to a total order. In this case, the minimum k -spanning acycle is unique with respect to the chosen total order, but its weights are independent of this choice ([39], Lemma 3.14). When $k = 1$, it corresponds to the definition of a minimum spanning tree: in particular, with the diameter as weight, we

have $\text{MST}(X) = \text{MSA}^1(\Delta(X)) = \text{MSA}^1(\text{DEL}(X))$. [Fig. 3](#), left, depicts minimum 1- and 2-spanning acycles for $X \subset \mathbb{R}^3$.

Minimum spanning acycles have only recently received significant attention, as they have interesting properties with birth and death values in persistence diagrams, as noticed in [\[39, 40\]](#). In particular, let $S \subset \mathcal{K}^k$ be a k -minimum spanning acycle for a weight function w . Then $\{w(\sigma) \mid \sigma \in S\}$ is the set of death times of the PH^{k-1} classes of the filtration induced by w on \mathcal{K} , while $\{w(\sigma) \mid \sigma \in \mathcal{K}^k \setminus S\}$ is the set of birth times of the PH^k classes. This is a generalization of the fact that the edges of the minimum spanning tree $\text{MST}(X)$ are exactly the edges killing the PH^0 classes of the (Delaunay)–Rips filtration of X (and that the remaining edges give birth to PH^1 classes). This is commonly used to speed up the computation of 0-dimensional persistence diagrams thanks to a union-find data structure [\[41\]](#).

Neighborhood graphs

The relative neighborhood graph [\[42\]](#) of X is defined as the set of edges $e = (x, y)$ such as there is no third point that is closer to x and y than they are to each other, i.e., $\text{RNG}(X) = \{(x, y) \in X^2 \mid \exists z \in X, d(x, z) < d(x, y) \text{ and } d(y, z) < d(x, y)\}$. It is a subgraph of the Delaunay complex which can be computed in time complexity $\mathcal{O}(n \log n)$ in the plane [\[43–45\]](#), but not in higher dimensions. Another graph of interest is the Urquhart graph $\text{UG}(X)$ [\[46\]](#) which is defined as the subgraph of the Delaunay complex where the longest edge of each Delaunay triangle has been removed. Under general position hypothesis, we have the inclusions $\text{MST}(X) \subseteq \text{RNG}(X) \subseteq \text{UG}(X) \subseteq \text{DEL}(X)$ (see [Fig. 3](#), right). It was showed in [\[21\]](#) that the edges of $\text{RNG}(X) \setminus \text{MST}(X)$ are exactly the edges that create a PH^1 pair of positive persistence for the Rips filtration of X .

4 Analysis

In this section, we establish how Delaunay–Rips persistence diagrams approximate Rips persistence diagrams, and what are the possible instabilities when the input is perturbed, both in theory and in practice.

Jung’s theorem [\[34\]](#) states that any compact set $K \subset \mathbb{R}^d$ of diameter $\delta(K) = \max_{x, y \in K} \|x - y\|_2$ is enclosed by a closed ball of radius $\text{meb}(K)$, with:

$$\delta(K) \leq 2 \text{meb}(K) \leq \delta(K) \underbrace{\sqrt{\frac{2d}{d+1}}}_{\triangleq j_d} \quad (9)$$

where the right inequality is precisely attained by the regular d -simplices. In addition, for any simplicial complex \mathcal{K} , any k -simplex $\sigma \in \mathcal{K}^k$ lives in a k -dimensional affine space, hence:

$$\delta(\sigma) \leq 2 \text{meb}(\sigma) \leq j_k \delta(\sigma). \quad (10)$$

Therefore, as the Čech and Delaunay–Čech filtrations writes respectively as $\check{\mathcal{C}}_r(X) = \{\sigma \subset X \mid \text{meb}(\sigma) \leq r\}$ and $\mathcal{D}\check{\mathcal{C}}_r(X) = \{\sigma \in \text{DEL}(X) \mid \text{meb}(\sigma) \leq r\}$, we have the

following inclusions between their k -dimensional skeletons:

$$\begin{aligned}\check{\mathcal{C}}_r^{(k)}(X) &\subset \mathcal{R}_r^{(k)}(X) \subset \check{\mathcal{C}}_{j_k r}^{(k)}(X) \\ \mathcal{D}\check{\mathcal{C}}_r^{(k)}(X) &\subset \mathcal{D}\mathcal{R}_r^{(k)}(X) \subset \mathcal{D}\check{\mathcal{C}}_{j_k r}^{(k)}(X).\end{aligned}\tag{11}$$

In addition, due to $\mathsf{DEL}(X) \subset \Delta(X)$, we also have the following inclusions:

$$\begin{aligned}\mathcal{D}\check{\mathcal{C}}_r^{(k)}(X) &\subset \check{\mathcal{C}}_r^{(k)}(X) \\ \mathcal{D}\mathcal{R}_r^{(k)}(X) &\subset \mathcal{R}_r^{(k)}(X).\end{aligned}\tag{12}$$

Applying the homology functor on these simplicial inclusions provides induced inclusions between the corresponding homology groups, for example, for the first one, $H^k(\check{\mathcal{C}}_r) \hookrightarrow H^k(\mathcal{R}_r) \hookrightarrow H^k(\check{\mathcal{C}}_{j_{k+1} r})$. In addition, $\check{\mathcal{C}}_r$ can be transformed into $\mathcal{D}\check{\mathcal{C}}_r$ with a sequence of elementary collapses [5]. On the homology level, this not only implies that $H^k(\mathcal{D}\check{\mathcal{C}}_r)$ and $H^k(\check{\mathcal{C}}_r)$ are isomorphic, but also (see e.g., [47]) that for all r , the simplicial inclusion $\iota : \mathcal{D}\check{\mathcal{C}}_r^{(k)} \hookrightarrow \check{\mathcal{C}}_r^{(k)}$ induces an isomorphism

$$\iota_* : H^k(\mathcal{D}\check{\mathcal{C}}_r) \xrightarrow{\cong} H^k(\check{\mathcal{C}}_r).\tag{13}$$

4.1 Rips and Delaunay–Rips comparison

Thanks to these relations, we can now show that the Delaunay–Rips persistence module provides an approximation of the Rips persistence module.

Theorem 1. *The k -dimensional Rips and Delaunay–Rips persistence modules $(H^k(\mathcal{R}_r))_{r \geq 0}$ and $(H^k(\mathcal{D}\mathcal{R}_r))_{r \geq 0}$ are multiplicatively, strongly j_{k+1} -interleaved. As a corollary, the strong stability theorem (see Sec. 3.2) states that:*

$$d_b \left(\log \text{dgm}_{\mathcal{D}\mathcal{R}}^k(X), \log \text{dgm}_{\mathcal{R}}^k(X) \right) \leq \log j_{k+1}.\tag{14}$$

Proof Using the included inclusions (Eq. 11, Eq. 12) and induced isomorphisms (Eq. 13) between homology groups, we can define linear maps $\Phi_r^k : H^k(\mathcal{R}_r) \rightarrow H^k(\mathcal{D}\mathcal{R}_{j_{k+1} r})$ as:

$$\Phi_r^k : H^k(\mathcal{R}_r) \hookrightarrow H^k(\check{\mathcal{C}}_{j_{k+1} r}) \xleftarrow[\iota_*^{-1}]{\iota_*} H^k(\mathcal{D}\check{\mathcal{C}}_{j_{k+1} r}) \hookrightarrow H^k(\mathcal{D}\mathcal{R}_{j_{k+1} r}).$$

Now, to show that the persistence modules $(H^k(\mathcal{R}_r))_{r \geq 0}$ and $(H^k(\mathcal{D}\mathcal{R}_r))_{r \geq 0}$ are multiplicatively j_{k+1} -interleaved, it suffices to notice that the following diagrams (on the homology groups level) commute:

$$\begin{array}{ccc}
H^k(\mathcal{DR}_r) \hookrightarrow H^k(\mathcal{DR}_{j_{k+1}r}) & & H^k(\mathcal{DR}_{j_{k+1}r}) \hookrightarrow H^k(\mathcal{DR}_{j_{k+1}r'}) \\
\downarrow & \nearrow \Phi_r^k & \Phi_r^k \nearrow \\
H^k(\mathcal{R}_r) & & H^k(\mathcal{R}_{r'}) \\
\\
\Phi_{r/j_{k+1}}^k \nearrow & H^k(\mathcal{DR}_r) & H^k(\mathcal{DR}_r) \hookrightarrow H^k(\mathcal{DR}_{r'}) \\
& \downarrow & \downarrow \\
H^k(\mathcal{R}_{r/j_{k+1}}) \hookrightarrow H^k(\mathcal{R}_r) & & H^k(\mathcal{R}_r) \hookrightarrow H^k(\mathcal{R}_{r'}) \\
\end{array}$$

To see that, one can decompose the diagrams following the expression of Φ_r^k . For instance, for the first diagram,

$$\begin{array}{ccc}
H^k(\mathcal{DR}_r) \hookrightarrow H^k(\mathcal{DR}_{j_{k+1}r}) & & \\
\downarrow & \nearrow \text{dashed} & \uparrow \\
& H^k(\mathcal{DC}_{j_{k+1}r}) & \\
\downarrow & \nearrow \simeq & \downarrow \simeq \\
& H^k(\check{\mathcal{C}}_{j_{k+1}r}) & \\
\downarrow & \nearrow & \\
H^k(\mathcal{R}_r) & &
\end{array}$$

commutes because its counterpart on the simplicial level commutes, and the induced isomorphic inclusion can be inverted while maintaining commutativity. The same applies to the second and third diagrams. \square

The bound [Eq. 14](#) is tight, since it is possible to find $X \subset \mathbb{R}^{d+1}$ such that $d_b(\log \text{dgm}_{\mathcal{DR}}^d(X), \log \text{dgm}_{\mathcal{R}}^d(X))$ is arbitrarily close to its upper bound $\log j_{d+1}$. For that, it suffices to take two antipodal points, e.g, $x_0 = (1, 0, \dots, 0)$ and $x_1 = (-1, 0, \dots, 0)$ that will be joined by a Delaunay edge, the points of a regular $(d+1)$ -simplex inscribed in $(1+\varepsilon)\mathbb{S}^d$, and finally a sufficiently dense sampling of $(1+\varepsilon)\mathbb{S}^d$ to ensure the existence of a PH^d class. It will be killed by the Delaunay edge $\{x_0, x_1\}$ of length 2 in the Delaunay–Rips filtration, and by an edge of the regular simplex of length $(1+\varepsilon)\sqrt{2(d+2)/(d+1)} = 2(1+\varepsilon)/j_{d+1}$ in the Rips filtration. Such configurations are shown for \mathbb{R}^2 and \mathbb{R}^3 in [Fig. 4](#), where the points are arranged respectively as a regular hexagon and a regular dodecahedron.

For the particular case of $k = 0$, [Eq. 14](#) gives more directly that 0-th Rips and Delaunay–Rips persistence modules are isomorphic, and thus that $\text{dgm}_{\mathcal{R}}^0(X) = \text{dgm}_{\mathcal{DR}}^0(X)$. In the other cases ($k \geq 1$), this only gives an upper bound of the bottleneck distance between logarithmic diagrams. In practice, one could be more interested by a bound between the persistence diagrams themselves. Unfortunately, such a bound has to scale with the diameter of point cloud X :

$$d_b(\text{dgm}_{\mathcal{DR}}^k(X), \text{dgm}_{\mathcal{R}}^k(X)) \leq (j_{k+1} - 1)\delta(X) \quad (15)$$

where $\delta(X) = \max_{x,y \in X} \|x - y\|_2$ is the diameter of X .

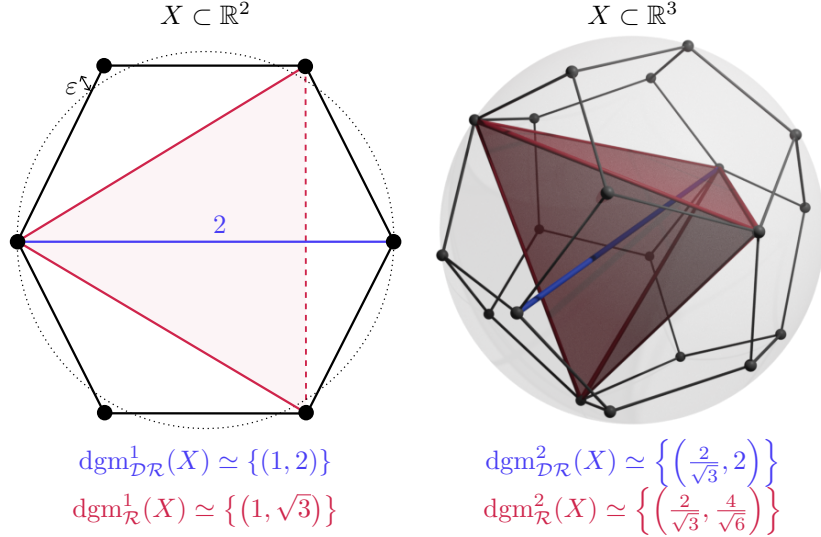


Fig. 4 **Left:** $X \subset \mathbb{R}^2$ such that $\text{d}_b(\log \text{dgm}_{\mathcal{DR}}^1(X), \log \text{dgm}_{\mathcal{R}}^1(X))$ is arbitrarily close to $\log \frac{2}{\sqrt{3}} = \log j_2$. The points are arranged as a regular hexagon inscribed in the unit circle, slightly perturbed so that its Delaunay triangulation (plain edges) contains a diametrical edge (blue edge). The red dotted edge that exists in $\Delta(X)$ but not in $\text{DEL}(X)$ makes the PH^1 class less persistent in the Rips filtration than in the Delaunay–Rips filtration. **Right:** $X \subset \mathbb{R}^3$ such that $\text{d}_b(\log \text{dgm}_{\mathcal{DR}}^2(X), \log \text{dgm}_{\mathcal{R}}^2(X))$ is arbitrarily close to $\log \frac{\sqrt{6}}{2} = \log j_3$. The points are arranged as a regular dodecahedron inscribed in the unit sphere, slightly perturbed so that its Delaunay triangulation contains a diametrical edge (blue edge). A non-Delaunay regular tetrahedron (in red) makes the PH^2 class less persistent in the Rips filtration than in the Delaunay–Rips filtration.

4.2 Delaunay–Rips instability

Now, with both [Eq. 7](#) and [Eq. 15](#), we can naively write with the triangle inequality the maximum instability that may happen next to a Delaunay non-general position:

$$\begin{aligned}
 \text{d}_b\left(\text{dgm}_{\mathcal{DR}}^k(X), \text{dgm}_{\mathcal{DR}}^k(Y)\right) &\leq \text{d}_b\left(\text{dgm}_{\mathcal{DR}}^k(X), \text{dgm}_{\mathcal{R}}^k(X)\right) \\
 &\quad + \text{d}_b\left(\text{dgm}_{\mathcal{R}}^k(X), \text{dgm}_{\mathcal{R}}^k(Y)\right) \\
 &\quad + \text{d}_b\left(\text{dgm}_{\mathcal{R}}^k(Y), \text{dgm}_{\mathcal{DR}}^k(Y)\right) \\
 &\leq (j_{k+1} - 1) (\delta(X) + \delta(Y)) + 2 \text{d}_{\text{GH}}(X, Y)
 \end{aligned} \tag{16}$$

However, this upper bound can be slightly improved by finding some interleaving relationships involving the Delaunay–Rips persistence modules of X and Y , with the following result.

Theorem 2. *Let X and Y two point clouds. Then for any dimension $k \geq 0$:*

$$\text{d}_b\left(\text{dgm}_{\mathcal{DR}}^k(X), \text{dgm}_{\mathcal{DR}}^k(Y)\right) \leq (j_{k+1} - 1) \max\{\delta(X), \delta(Y)\} + 2 \text{d}_{\text{GH}}(X, Y). \tag{17}$$

Proof Let $k \geq 0$ be a fixed homology dimension and $\eta = j_{k+1}$. Let also $\varepsilon > 2d_{\text{GH}}(X, Y)$. We know that $(H(\check{C}_r(X)))_{r \geq 0}$ and $(H(\check{C}_r(Y)))_{r \geq 0}$ are ε -interleaved (see Lemma 4.4 of [36]). We write $\alpha_r : H(\check{C}_r(X)) \rightarrow H(\check{C}_{r+\varepsilon}(Y))$ and $\beta_r : H(\check{C}_r(Y)) \rightarrow H(\check{C}_{r+\varepsilon}(X))$ the corresponding linear maps. In addition to the induced inclusions (Eq. 11, Eq. 12) and induced isomorphisms (Eq. 13), they permit to define the following linear maps (we write $K_r(X)$ instead of $H^k(\mathcal{DR}_r(X))$ to simplify the notations):

$$\Phi_r : K_r(X) \hookrightarrow H^k(\check{C}_{\eta r}(X)) \xrightarrow{\alpha_{\eta r}} H^k(\check{C}_{\eta r+\varepsilon}(Y)) \xleftarrow[\iota_{\star}^{-1}]{} H^k(\mathcal{D}\check{C}_{\eta r+\varepsilon}(Y)) \hookrightarrow K_{\eta r+\varepsilon}(Y)$$

$$\Psi_r : K_r(Y) \hookrightarrow H^k(\check{C}_{\eta r}(Y)) \xrightarrow{\beta_{\eta r}} H^k(\check{C}_{\eta r+\varepsilon}(X)) \xleftarrow[\iota_{\star}^{-1}]{} H^k(\mathcal{D}\check{C}_{\eta r+\varepsilon}(X)) \hookrightarrow K_{\eta r+\varepsilon}(X)$$

Now, we notice that the following diagrams involving these two maps commute:

$$\begin{array}{ccc} K_{(r-\varepsilon)/\eta}(X) & \xrightarrow{\quad} & K_{\eta r+\varepsilon}(X) \\ \Phi_{(r-\varepsilon)/\eta} \searrow & & \nearrow \Psi_r \\ K_r(Y) & \xrightarrow{\quad} & K_{\eta r+\varepsilon}(X) \\ & & \uparrow \Psi_r \\ & & K_{\eta r+\varepsilon}(X) \hookrightarrow K_{\eta r'+\varepsilon}(X) \\ & & \nearrow \Psi_{r'} \\ & & K_r(Y) \hookrightarrow K_{r'}(Y) \\ & & \nearrow \Psi_{r'} \\ & & K_{\eta r'+\varepsilon}(X) \end{array}$$

$$\begin{array}{ccc} & & K_{\eta r+\varepsilon}(X) \hookrightarrow K_{\eta r'+\varepsilon}(X) \\ & & \nearrow \Psi_{r'} \\ & & K_r(Y) \hookrightarrow K_{r'}(Y) \\ & & \nearrow \Psi_{r'} \\ K_{(r-\varepsilon)/\eta}(X) & \xrightarrow{\quad} & K_{\eta r+\varepsilon}(Y) \\ \Psi_{(r-\varepsilon)/\eta} \nearrow & & \searrow \Phi_r \\ K_{(r-\varepsilon)/\eta}(Y) & \xrightarrow{\quad} & K_{\eta r+\varepsilon}(Y) \end{array}$$

To see that, as in Th. 1, we can decompose the diagrams following the expressions of Φ and Ψ . For instance, for the first diagram,

$$\begin{array}{ccc} H^k(\mathcal{DR}_{(r-\varepsilon)/\eta}(X)) & \xrightarrow{\quad} & H^k(\mathcal{DR}_{\eta r+\varepsilon}(X)) \\ \downarrow & & \uparrow \\ & & H^k(\mathcal{D}\check{C}_{\eta r+\varepsilon}(X)) \\ \downarrow & & \downarrow \simeq \\ H^k(\check{C}_{r-\varepsilon}(X)) & \xrightarrow{\quad} & H^k(\check{C}_{\eta r+\varepsilon}(X)) \\ \alpha_{r-\varepsilon} \searrow & & \nearrow \beta_{\eta r} \\ H^k(\check{C}_r(Y)) & \xrightarrow{\quad} & H^k(\check{C}_{\eta r}(Y)) \\ \simeq \uparrow & & \nearrow \\ H^k(\mathcal{D}\check{C}_r(Y)) & & \\ \downarrow & & \\ H^k(\mathcal{DR}_r(Y)) & & \end{array}$$

commutes: for the top and bottom part, because it is the case for its counterpart on the simplicial level; for the central part, because this corresponds to the ε -interleaving between $(H(\check{C}_r(X)))_{r \geq 0}$ and $(H(\check{C}_r(Y)))_{r \geq 0}$. Then the isomorphic inclusions can be inverted while maintaining commutativity.

Now, we rescale those persistence modules so that we get a usable additive interleaving. Let $f : r \mapsto \log \left(r + \frac{\varepsilon}{\eta-1} \right)$, which is chosen so that:

$$\begin{aligned} f(\eta r + \varepsilon) &= \log \left(\eta r + \varepsilon + \frac{\varepsilon}{\eta-1} \right) \\ &= \log \left(\eta \left(r + \frac{\varepsilon}{\eta-1} \right) \right) \\ &= f(r) + \log \eta \end{aligned}$$

Therefore, with the four commutative diagrams above, the modules $(K_{f^{-1}(\alpha)}(X))_\alpha$ and $(K_{f^{-1}(\alpha)}(Y))_\alpha$ are additively $(\log \eta)$ -interleaved. With the strong stability theorem [32], we obtain that the image through f of the diagrams $\text{dgm}_{\mathcal{DR}}^k(X)$ and $\text{dgm}_{\mathcal{DR}}^k(Y)$ have their bottleneck distance bounded by $\log \eta$, i.e.,

$$d_b(f(\text{dgm}_{\mathcal{DR}}^k(X)), f(\text{dgm}_{\mathcal{DR}}^k(Y))) \leq \log \eta \text{ where } f(D) = \{(f(b), f(d)) \mid (b, d) \in D\}. \quad (18)$$

Eventually, let $p = (x, y) \in \text{dgm}_{\mathcal{DR}}^k(X) \cup \Delta$ and $p' = (x', y') \in \text{dgm}_{\mathcal{DR}}^k(Y) \cup \Delta$, where $\Delta = \{(x, x) \mid x \geq 0\}$ is the diagonal, such that $f(p)$ and $f(p')$ are paired together in an optimal pairing for Eq. 18. We have for x and x' (this is the same for y and y'):

$$\begin{aligned} |f(x) - f(x')| &\leq \log \eta \\ \left| \log \left(x + \frac{\varepsilon}{\eta-1} \right) - \log \left(x' + \frac{\varepsilon}{\eta-1} \right) \right| &\leq \log \eta \\ \left| \log \frac{x + \frac{\varepsilon}{\eta-1}}{x' + \frac{\varepsilon}{\eta-1}} \right| &\leq \log \eta \\ \frac{1}{\eta} \leq \frac{x + \frac{\varepsilon}{\eta-1}}{x' + \frac{\varepsilon}{\eta-1}} &\leq \eta \end{aligned}$$

Therefore:

$$\begin{aligned} x + \frac{\varepsilon}{\eta-1} &\leq \eta x' + \frac{\eta \varepsilon}{\eta-1} \quad \text{and} \quad x' + \frac{\varepsilon}{\eta-1} \leq \eta x + \frac{\eta \varepsilon}{\eta-1} \\ x - x' &\leq (\eta - 1)x' + \varepsilon \quad \text{and} \quad x' - x \leq (\eta - 1)x + \varepsilon \end{aligned}$$

Thus, $|x - x'| \leq (\eta - 1) \max\{x, x'\} + \varepsilon$, and similarly for y and y' . Hence,

$$\|p - p'\|_\infty \leq (\eta - 1) \max\{\|p\|_\infty, \|p'\|_\infty\} + \varepsilon \leq (\eta - 1) \max\{\delta(X), \delta(Y)\} + \varepsilon$$

since coordinates in a Delaunay–Rips persistence diagram corresponds to edge lengths. Thus $\|p\|_\infty \leq \delta(X)$ for all $p \in \text{dgm}_{\mathcal{DR}}^k(X)$. Therefore, using such an optimal pairing for Eq. 18 in order to pair $\text{dgm}_{\mathcal{DR}}^k(X)$ and $\text{dgm}_{\mathcal{DR}}^k(Y)$ together shows that $d_b(\text{dgm}_{\mathcal{DR}}^k(X), \text{dgm}_{\mathcal{DR}}^k(Y)) \leq (\eta - 1) \max\{\delta(X), \delta(Y)\} + \varepsilon$, which concludes the proof. \square

4.3 Approximation and stability in practice

We show in Fig. 5 the distribution of the bottleneck distance between Rips and Delaunay–Rips logarithmic 1- and 2-dimensional persistence diagrams for points in \mathbb{R}^3 with several distributions. This illustrates that the bound Eq. 15 is pessimistic for uniformly sampled points (left), while PH¹ and PH² bounds can be closely reached for points sampled respectively on a circle (center) and a sphere (right), which correspond to the critical configurations described in Sec. 4.1 and Fig. 4.

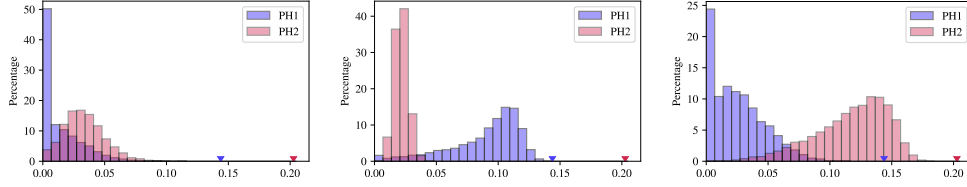


Fig. 5 Histograms of the distribution of the bottleneck distance between logarithmic persistence diagrams for the Rips and Delaunay–Rips filtrations. Triangles indicates the theoretical upper bound of these distances for a given dimension of homology. **Left:** 10000 sets of 50 points uniformly distributed in $[0, 1]^3$. **Center:** 10000 sets of 50 points distributed on a unit circle embedded in \mathbb{R}^3 with Gaussian noise. **Right:** 10000 sets of 50 points uniformly distributed on a unit 2-sphere with Gaussian noise.

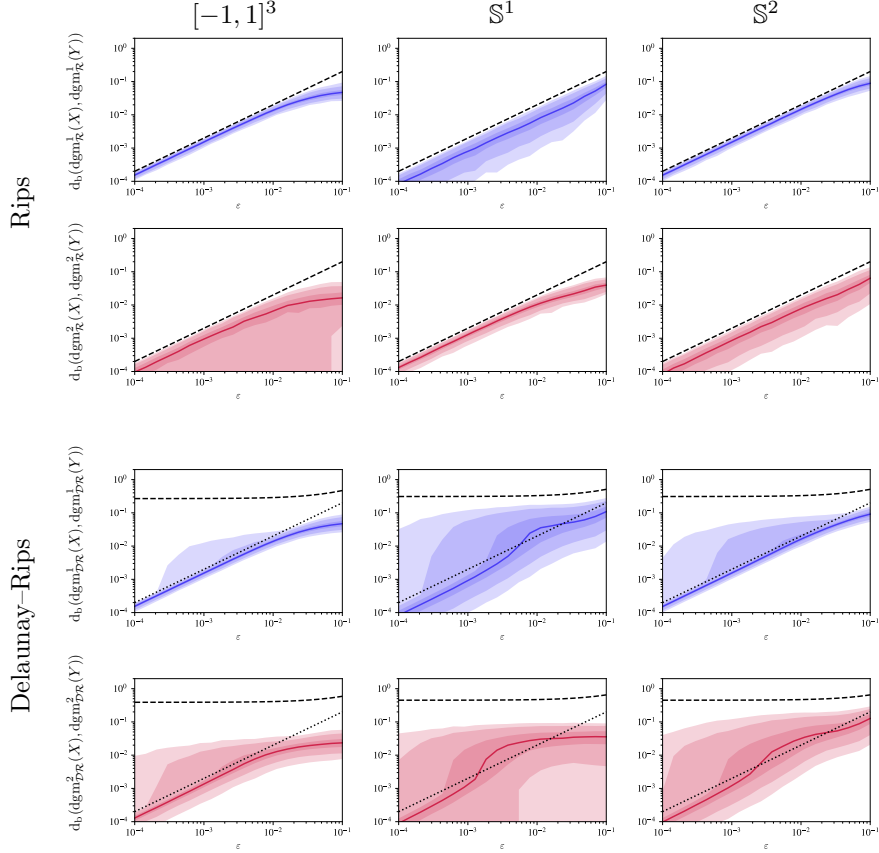


Fig. 6 Distribution of the bottleneck distance between Rips or Delaunay–Rips 1- and 2-dimensional persistence diagrams of two point clouds X and $Y \subset \mathbb{R}^3$ where $d_{\text{GH}}(X, Y) \leq \varepsilon$. The left column corresponds to X uniformly sampled in $[-1, 1]^3$, the center one to X sampled next to unit circle, and the right one to X sampled next to the unit sphere. The dashed, black line corresponds to Eq. 17 for the Delaunay–Rips filtration charts, and to Eq. 7 (i.e., $\mathcal{W}_\infty \leq 2\varepsilon$) for the Rips filtration charts. The distributions are represented with their median (plain lines) and their 0.01-, 0.05- and 0.25-quantiles (areas with three color shades).

In [Fig. 6](#) we compare the empiric stability of Rips ([Eq. 7](#)) and Delaunay–Rips ([Eq. 16](#)) persistence diagrams to perturbations on the input. Contrary to the Rips case, using the Delaunay–Rips filtration can lead to a bottleneck distance beyond $2 d_{\text{GH}}(X, Y)$ due to the term $\max\{\delta(X), \delta(Y)\}$ in [Eq. 17](#) that depends on X and Y directly rather than $d_{\text{GH}}(X, Y)$. Once again, this instability is worse for points distributed close to a circle or a sphere as this corresponds to the critical configurations described in [Sec. 4.1](#) and [Fig. 4](#).

Thus, in practice, the continuity of Delaunay–Rips persistence diagrams should not be assumed for applications, even though discontinuities informally depend on the presence of extreme and neat topological features (e.g., a dense sampling exactly on a circle or a sphere). Moreover, given a point cloud, Delaunay–Rips persistence diagrams still capture topological information that is close to that captured by Rips persistence diagrams, up to the size of the point cloud. This suggests an explanation for its usability for diverse applications as mentioned in [\[6\]](#) (topological prior incorporation) or [\[7\]](#) (classification) which does not depend on a continuity assumption.

5 Algorithm

In this section, we introduce an algorithm specifically dedicated to the computation of Delaunay–Rips persistence diagrams. We begin with a few definitions and lemmas ([Sec. 5.1](#)), before presenting the algorithm ([Sec. 5.2](#)) and how it can be implemented ([Sec. 5.3](#), [Sec. 5.4](#)).

5.1 Generalities

Let $X \subset \mathbb{R}^d$ and \mathcal{K} either $\text{DEL}(X)$ or $\Delta(X)$. For each $k \geq 1$, we build a total order \prec_k on \mathcal{K}^k that extends the partial order induced by the diameter, i.e., for all $\sigma, \sigma' \in \mathcal{K}^k$, if $\delta(\sigma) < \delta(\sigma')$, then $\sigma \prec_k \sigma'$. More precisely, we define by recurrence on $k \geq 1$:

$$\begin{aligned} \sigma \prec_1 \sigma' &\iff \delta(\sigma) < \delta(\sigma') \text{ or } (\delta(\sigma) = \delta(\sigma') \text{ and } \sigma \prec_{\text{lex}} \sigma') \\ \sigma \prec_{k+1} \sigma' &\iff \max \partial\sigma \prec_k \max \partial\sigma' \text{ or } (\max \partial\sigma = \max \partial\sigma' \text{ and } \sigma \prec_{\text{lex}} \sigma') \end{aligned} \quad (19)$$

where \max is understood as with respect to \prec_k and where \prec_{lex} is the lexicographic order between simplices sorted with increasing vertices. In the following, we write more consisely \prec instead of \prec_k as k is given by σ and σ' .

As mentioned in [Sec. 3.5](#), the minimum k -spanning acycle is unique with respect to the chosen total order [\[39\]](#) (even though the diameters of the simplices it contains is independent of this choice), so that we write in the following $\text{MSA}^k(X)$. We omit specifying X when this is unambiguous.

We define below the k -dimensional relative neighborhood simplices RNS^k , for $1 \leq k < d$:

$$\text{RNS}^k(\mathcal{K}) = \{\sigma \in \mathcal{K}^k \mid \forall \tau \in \text{cof}(\sigma, \mathcal{K}), \sigma \prec \max \partial\tau\} \quad (20)$$

where $\text{cof}(\sigma, \mathcal{K}) = \{\tau \in \mathcal{K} \mid \sigma \subset \tau \text{ and } \dim \tau = \dim \sigma + 1\}$ is the set of cofacets of a simplex σ in \mathcal{K} . This construction offers a generalization – in terms of dimension k –

of both Urquhart and relative neighborhood graphs, as $\text{UG}(X) = \text{RNS}^1(\text{DEL}(X))$ and $\text{RNG}(X) = \text{RNS}^1(\Delta(X))$. As we focus on the Delaunay–Rips filtration, we now set $\mathcal{K} = \text{DEL}(X)$ and we note more concisely the k -dimensional Urquhart simplices $\text{US}^k(X) = \text{RNS}^k(\text{DEL}(X))$ (see example in Fig. 7).

An apparent pair [1] is a pair (σ, τ) such that σ is the youngest facet of τ and τ is the oldest cofacet of σ . Note that any apparent pair is indeed a persistent pair (see Lemma 3.3 of [1]). In addition, for filtrations based on the diameter (e.g., Rips or Delaunay–Rips filtrations), any k -dimensional apparent pair (σ, τ) , with $k \geq 1$, has persistence zero, since in this case $\delta(\tau) = \max_{\sigma' \in \partial\tau} \delta(\sigma') = \delta(\sigma)$. In the following we call *zero* (resp. *positive*) *persistent pairs* the persistent pairs of persistence zero (resp. of positive persistence). We show below some links that the above construction has with (apparent) zero and positive persistence pairs. Before that, we first cite a lemma that will be useful in the following.

Lemma 1 (Exchange property, see Lemma 3.7 of [39]). *Let $S \subset \mathcal{K}^k$ be a k -spanning acycle of \mathcal{K} and $\sigma \in \mathcal{K}^k \setminus S$. For any $\sigma' \in S$ such that σ' is part of a k -cycle containing σ , $S \cup \{\sigma\} \setminus \{\sigma'\}$ is also a k -spanning acycle of \mathcal{K} .*

The following result generalizes the fact that in general position, MST is included in both RNG and UG (see Sec. 3.5).

Lemma 2. *For all $1 \leq k < d$, $\text{MSA}^k \subset \text{US}^k$.*

Proof Let $\sigma \in \text{MSA}^k$. Suppose that $\sigma \notin \text{US}^k$. By definition, there exists $\tau \in \text{cof}(\sigma, \text{DEL})$ such that $\sigma = \max \partial\tau$. Now, there exists a $\sigma' \in \partial\tau \setminus \{\sigma\}$ such that $\sigma' \notin \text{MSA}^k$ (otherwise $\partial\tau$ would constitute a k -cycle in MSA^k , which is acyclic). According to the exchange property of spanning acycles (Lem. 1), $\text{MSA}^k \cup \{\sigma'\} \setminus \{\sigma\}$ is also a k -spanning acycle, with $\sigma' \prec \sigma$, which contradicts the minimality of MSA^k . \square

Lemma 3. *All k -simplices that give birth to a positive k -dimensional persistent pair are contained in $\text{US}^k \setminus \text{MSA}^k$.*

Proof Let $\sigma \in \text{DEL}^k$ such that $\sigma \notin \text{US}^k$. By definition, there exists at least one $\tau \in \text{cof}(\sigma, \text{DEL})$ such that $\sigma = \max \partial\tau$. Let τ^* the first of them that appears in the filtration (i.e., the smallest for \prec). Then, by definition, (σ, τ^*) is an apparent PH^k pair, and therefore a zero persistence pair. Therefore, a k -simplex that gives birth to a positive PH^k pair is necessarily in US^k . In addition, a k -simplex in MSA^k corresponds to the death of a PH^{k-1} pair, therefore not to the birth of a PH^k pair, hence the result. \square

We can establish a more precise result for PH^1 . Indeed, it is established in [21] that, for the Rips filtration, the edges in $\text{RNG} \setminus \text{MST}$ exactly correspond to the births of the positive PH^1 pairs. We establish below an analogous result for the Delaunay–Rips filtration, involving UG instead of RNG .

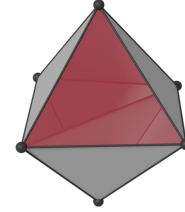


Fig. 7 US^2 , with $\text{US}^2 \setminus \text{MSA}^2$ in transparent red.

Lemma 4 (Theorem 3.10 of [1]). *Let X with distinct pairwise distances. Among the PH^1 pairs, the apparent pairs are exactly the zero persistence pairs.*

Lemma 5. *Let X in general position (unique pairwise distances, in addition to the general position for the Delaunay complex). The edges in $\text{UG} \setminus \text{MST}$ exactly correspond to the births of PH^1 pairs with a positive persistence for the Delaunay–Rips filtration.*

Proof Recall that $\text{US}^1 = \text{UG}$ and $\text{MSA}^1 = \text{MST}$. Hence, Lem. 3 gives that the edges giving birth to a positive PH^1 pair are in $\text{UG} \setminus \text{MST}$. Reciprocally, if (σ, τ) is a zero persistence PH^1 pair, Lem. 4 states that it is an apparent pair. Then $\sigma \subset \tau$ and $\sigma = \max \partial\tau$. Therefore $\sigma \notin \text{UG}$, hence the result. \square

Finally, the choice made for the total order (Eq. 19) enables the following result:

Lemma 6. *Let σ be k -simplex. If $\sigma \prec \max \partial\tau$ for all $\tau \in \text{cof}(\sigma, \text{MSA}^{k+1})$, then $\sigma \in \text{US}^k$. In other words, to determine whether a simplex is in US^k , it suffices to check if it is not the largest facet of any of its cofacets in MSA^{k+1} (instead of all its cofacets).*

Proof Suppose by contradiction that we have a k -simplex σ that verifies this condition, but such that $\sigma \notin \text{US}^k$. This means that there exists a $\tau^* \in \text{cof}(\sigma)$ such that $\sigma = \max \partial\tau^*$. However, by hypothesis, any $\tau \in \text{cof}(\sigma, \text{MSA}^{k+1})$ verifies $\sigma \prec \max \partial\tau$, which implies here that $\tau^* \notin \text{MSA}^{k+1}$. In addition, as MSA^{k+1} is spanning, there exists a $\tau' \in \text{cof}(\sigma, \text{MSA}^{k+1})$, which therefore verifies $\sigma \prec \max \partial\tau'$. Thus, we have $\max \partial\tau^* \prec \max \partial\tau'$, hence $\tau^* \prec \tau'$ (see Eq. 19). With the exchange property (Lem. 1), $\text{MSA}^{k+1} \cup \{\tau^*\} \setminus \{\tau'\}$ is a $(k+1)$ -spanning acycle with $\tau^* \prec \tau'$, which contradicts the minimality of MSA^{k+1} . \square

5.2 Description

In this section, we turn to the description of an algorithm that computes the persistence diagrams of the Delaunay–Rips filtration of a point cloud in arbitrary dimension. The idea is to gather k -simplices into k -cells delimited by US^{k-1} in order to reduce the number of reduction steps in the computation of PH^{k-1} .

5.2.1 Codimension-1 persistent homology

For the specific case of persistent homology of codimension 1 (i.e., PH^{d-1}), we can rely on a duality approach. For that, recall that Lem. 3 means that the simplices that are not in US^{d-1} correspond to births of apparent, zero PH^{d-1} pairs. To determine the non-apparent PH^{d-1} pairs, we consider the d -cells delimited by US^{d-1} (they geometrically correspond to d -polytopes). We can endow each of them with the diameter of largest Delaunay simplex they contain, as filtration value. Then, by duality, finding PH^{d-1} is equivalent to computing PH^0 of the dual graph where dual nodes are these d -cells and dual edges are the US^{d-1} simplices between them, with all weights set to their opposite value. All US^{d-1} simplices that are unpaired at the end of the reduction gives MSA^{d-1} . Note that this is equivalent to performing a reverse–delete algorithm on US^{d-1} to obtain MSA^{d-1} (like minimum spanning trees, minimum spanning acycles can be computed thanks to greedy algorithms like Kruskal’s or reverse–delete [39]).

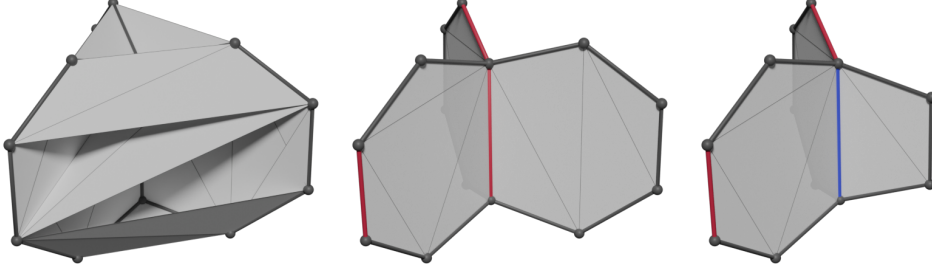


Fig. 8 **Left:** A point cloud $X \subset \mathbb{R}^3$ and its MSA^2 , with UG highlighted. **Center:** This point cloud has three PH^1 positive persistent pairs. The three edges in $\text{UG} \setminus \text{MST}$ are in red (one of them is also in NM^1). The edges of the MST are the black and thick edges. **Right:** Same thing, but with only two PH^1 positive persistent pairs. However, here, there is an edge in $\text{NM}^1 \setminus \text{UG}$, shown in blue. Thus, three finite polygons are still considered in MSA^2 , and one of them will give an apparent pair.

5.2.2 Intermediate persistent homologies

For computing PH^k , with $1 \leq k \leq d - 2$, we follow the same strategy to ignore zero persistent pairs, i.e., by gathering $(k + 1)$ -simplices into $(k + 1)$ -cells. The first step is to establish US^k that can be obtained from MSA^{k+1} thanks to [Lem. 6](#). However, unlike the codimension-1 case, US^k does not unambiguously define $(k + 1)$ -cells within MSA^{k+1} , since the latter has a non-manifold structure. Indeed, it contains k -simplices that are connected to more than two $(k + 1)$ -simplices (see [Fig. 8](#) for $d = 3$ and $k = 1$). We define those *non-manifold* k -simplices as:

$$\text{NM}^k = \left\{ \sigma \in \text{DEL}^k \mid |\text{cof}(\sigma, \text{MSA}^{k+1})| > 2 \right\}. \quad (21)$$

Then, we rather consider the $(k + 1)$ -cells that are – this time unambiguously – delimited within MSA^k by the union $\text{US}^k \cup \text{NM}^k$, at the price of dealing with some additional apparent pairs (exactly $|\text{NM}^k \setminus \text{US}^k|$). These $(k + 1)$ -cells are given as filtration value the diameter of the largest simplex they contain. Pairing them with $\text{US}^k \cup \text{NM}^k$ gives PH^k . The k -simplices that are still unpaired at the end of the reduction exactly gives MSA^k . [Alg. 1](#) gives an overview of the algorithm and [Sec. 5.3](#) describes more precisely each step and the data structures they use.

Algorithm 1: Obtain PH^k from PH^{k+1}

Input: Point cloud $X \subset \mathbb{R}^d$, MSA^{k+1}

Output: $\text{dgm}_{\mathcal{DR}}^k$ and MSA^k

- 1 Compute US^k and non-manifold simplices NM^k in MSA^{k+1}
- 2 Determine the $(k + 1)$ -cells formed by $\text{US}^k \cup \text{NM}^k$ within MSA^{k+1}
- 3 Pair those $(k + 1)$ -cells with the k -simplices in $\text{US}^k \cup \text{NM}^k$ to obtain $\text{dgm}_{\mathcal{DR}}^k$
- 4 MSA^k is given by the k -simplices in US^k that are still unpaired

5.2.3 1-dimensional persistent homology

For the specific case of 1-dimensional persistent homology, we can exploit the additional knowledge of the edges that give birth to PH^1 pairs before the reduction. Indeed, among $\text{UG} \cup \text{NM}^1$ edges, only those in $(\text{UG} \cup \text{NM}^1) \setminus \text{MST}$ are creating PH^1 pairs. Therefore, during the reduction, we can only consider the latters in the boundaries. [Alg. 2](#) gives an overview of the algorithm and [Sec. 5.3](#) describes more precisely each step and the data structures they use.

Note that for the specific context of $X \subset \mathbb{R}^3$, only the codimension-1 case (for PH^2 , see [Sec. 5.2.1](#)) and this 1-dimensional case (for PH^1 and PH^0) is required.

Algorithm 2: Obtain PH^0 and PH^1

Input: Point cloud $X \subset \mathbb{R}^d$, MSA^2

Output: Persistence diagrams $\text{dgm}_{\mathcal{DR}}^0$ and $\text{dgm}_{\mathcal{DR}}^1$

- 1 Extract UG and NM^1 from MSA^2 (see [Lem. 6](#))
- 2 Apply Kruskal's algorithm on UG to compute MST and $\text{dgm}_{\mathcal{DR}}^0$
- 3 Determine the polygons formed by $\text{UG} \cup \text{NM}^1$ in MSA^2
- 4 Pair those polygons with $(\text{UG} \cup \text{NM}^1) \setminus \text{MST}$ edges to obtain $\text{dgm}_{\mathcal{DR}}^1$

5.3 Data structures

We describe below more precisely each step of the algorithms described in [Sec. 5.2](#) and the data structures they use.

Delaunay complex

We use CGAL [48] to compute the Delaunay complex of $X \in \mathbb{R}^d$, with identifiers on vertices and *full cells*, and a virtual point at infinity to deal with its boundary (i.e., the border of the convex hull of X). This implementation offers the possibility to construct the Delaunay complex in parallel only for $d = 3$.

Urquhart facets and cells

US^{d-1} is built by enumerating the Delaunay $(d-1)$ -simplices and checking the local condition that they are not the largest (for \prec) facet of one of its adjacent d -simplices (see [Eq. 20](#)). During this computation, we maintain a union-find data structure on the d -simplices that enables deducing efficiently the *Urquhart d -cells* delimited by US^{d-1} . More precisely, when we encounter a non- US^{d-1} simplex, we merge the two classes associated with its (at most two) cofacets. At the end of the computation, the Urquhart d -cells are implicitly represented by the roots on this union-find data structure. In addition, for each class, we retrieve the largest d -simplex it contains.

Codimension-1 persistent pairs

Computing PH^{d-1} involves pairing the above Urquhart d -cells with the US^{d-1} simplices, which can be solved by relying on duality. Indeed, we can rather compute PH^0

of the dual graph where dual nodes are the Urquhart cells with the opposite diameter of their largest inner d -simplex as filtration value, and where dual edges are the \mathbf{US}^{d-1} simplices with their opposite diameter as filtration value. Simultaneously, we construct \mathbf{MSA}^{d-1} as the $(d-1)$ -simplices whose cofacets are already in the same union-find class (as deleting them would create a $(d-1)$ -cycle).

Other persistent pairs

We can compute \mathbf{US}^k by enumerating the k -simplices in \mathbf{MSA}^{k+1} (i.e., all the Delaunay k -simplices, since it is spanning). Leveraging [Lem. 6](#), it suffices to check the local condition that they are not the largest facet of one of their cofacets in \mathbf{MSA}^{k+1} . We also store the connectivity from k -simplices to \mathbf{MSA}^{k+1} simplices in a hash table. To handle the non-manifold structure of \mathbf{MSA}^{k+1} , we also determine the k -simplices in \mathbf{NM}^k (those with more than two cofacets, see [Eq. 21](#) and [Fig. 8](#)). Now, we can construct the *Urquhart* $(k+1)$ -cells, delimited by $\mathbf{US}^k \cup \mathbf{NM}^k$ within \mathbf{MSA}^{k+1} . For that, like in the codimesion-1 case, we maintain a union-find data structure over the \mathbf{MSA}^{k+1} simplices. When encountering a simplex that is not in $\mathbf{US}^k \cup \mathbf{NM}^k$, we merge the two union-find classes associated with its (at most two) cofacets. We also retrieve for each class the largest $(k+1)$ -simplex it contains. Finally, a reduction procedure permits to obtain \mathbf{PH}^k by pairing the Urquhart $(k+1)$ -cells with simplices in $\mathbf{US}^k \cup \mathbf{NM}^k$. This corresponds to [Alg. 1](#).

0- and 1-dimensional persistent pairs

Additionally, in the specific case where $k = 1$, we apply Kruskal's algorithm on $\mathbf{US}^1 = \mathbf{UG}$ to obtain \mathbf{MST} (of which $\mathrm{dgm}_{\mathcal{DR}}^0(X)$ can be deduced). Then, we can only consider the edges in $(\mathbf{UG} \cup \mathbf{NM}^1) \setminus \mathbf{MST}$ in the boundaries in the reduction procedure that pairs *Urquhart polygons* with these edges. This corresponds to [Alg. 2](#).

5.4 Parallelization

Algorithms [1](#) and [2](#) described above can be parallelized. Apart from the easily parallelizable tasks (traversals, sorting), three steps in particular require special care. First, establishing connectivity between k - and $(k-1)$ -simplices in \mathbf{MSA}^k can be done in parallel using a concurrent hash table implementation. Second, computing Urquhart cells can be done in parallel using a concurrent version of the union-find data structure, using wait-free algorithms that rely on CAS (compare-and-swap) operations [\[49\]](#). Finally, the reduction step that pairs k -cells with $(k-1)$ -simplices can also be done in parallel [\[9, 50\]](#): when a persistence pair (σ, τ) is created, it is temporary. If another thread later wants to pair σ with a τ' such that $\tau' \prec \tau$, then (σ, τ) is updated into (σ, τ') and the reduction of τ restarts.

6 Results

All results were obtained on a laptop computer with 64 GB of RAM and a Core i7-13850HX CPU (8 cores at 5.3 GHz and 12 cores at 3.8 GHz). We implemented our method in C++. For computing Delaunay complexes, we used the implementations

of CGAL [51], either specialized for \mathbb{R}^3 [48] or for arbitrary dimension [28]. Only the specialization to \mathbb{R}^3 benefits from an optional parallel implementation. However, this parallelization is not always advantageous, and can even be slower than the single-threaded version depending on the distribution of points in X .

Compared methods

We compared our approach with PHAT [52] and Gudhi [53]. For PHAT, the Delaunay triangulation is built with CGAL, then the boundary matrix is built with a code adapted from an add-on in the PHAT repository for computing persistence diagrams of α -filtrations [54], and finally reduced with the default algorithm and data structure provided by PHAT. For Gudhi, a simplex tree containing the Delaunay complex is built with the α -complex module [55] (without computing minimum enclosing balls), then the filtration values are set on the edges (i.e., their length) before being propagated to the rest of the simplices, and the persistence diagram is computed with the persistent cohomology module [56]. Finally, giotto-tda [8] computes the Delaunay complex with the implementation of Scipy [57] and passes the sparse distance matrix of Delaunay edges to Ripser [1] which computes the Rips persistent homology on this Delaunay complex. However, we did not include it in our comparison because it produces incorrect persistence diagrams and crashes when n is too high due to an internal limitation on simplex indices.

Performance

Fig. 9 compares the running time of our method specific to \mathbb{R}^3 , on point clouds distributed uniformly in the unit cube (left), on the unit circle (center) with some Gaussian noise for the circle. In order to compare with the Rips filtration, we also measured the running time of Ripser [1] for computing the 0-, 1-, and 2-dimensional persistence diagrams, showing – as expected – a much worse asymptotic behavior. For completeness, we also measured the running time of Euclidean PH1 [21], a method that computes 1-dimensional persistence diagrams of point clouds in \mathbb{R}^3 . Fig. 10 does the same comparison on uniformly distributed points clouds in \mathbb{R}^d , $4 \leq d \leq 8$. Tab. 1 shows the average running time ratio (with and without including the Delaunay complex computation step) and memory consumption ratio between our method and PHAT, by dimension. Overall, we observe that the running time ratio between our method and PHAT increases from 0.30 to 0.76 as d increases from 3 to 8. If we consider the Delaunay complex as the entry and omit its computation in the running time, the corresponding acceleration ratio varies from 0.20 to 0.73. Thus, our acceleration becomes less important as the dimension increases. Note that our implementation becomes noncompetitive for $d \geq 9$. In fact, $d = 9$ is already substantial for computing Delaunay complexes (which, for only 200 points, requires approximately 40 seconds and 850 MB of memory). Finally, our method uses between 0.19 and 0.35 times the memory used by PHAT.

Parallelism

Fig. 11 gives the speedup of the computation of the persistence diagrams with our parallel implementation (see Sec. 5.4) according to the number of threads. Note that

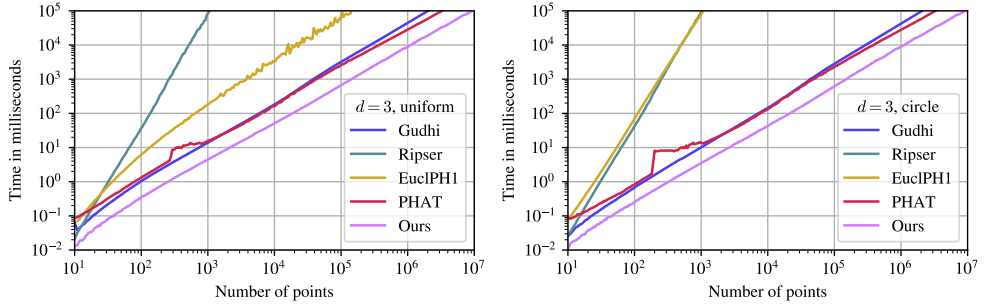


Fig. 9 Running time for computing the Delaunay–Rips persistence diagram of a point cloud in \mathbb{R}^3 , uniformly distributed in the unit cube (left) and next over the unit circle (right). We compare our approach described in Sec. 5 with Gudhi [53] and PHAT [52]. The running time for computing the Rips 0, 1 and 2-dimensional persistence diagrams with Ripser [1], and that for computing the Rips 0 and 1-dimensional persistence diagram with Euclidean PH1, the method described in [21], are also shown for comparison.

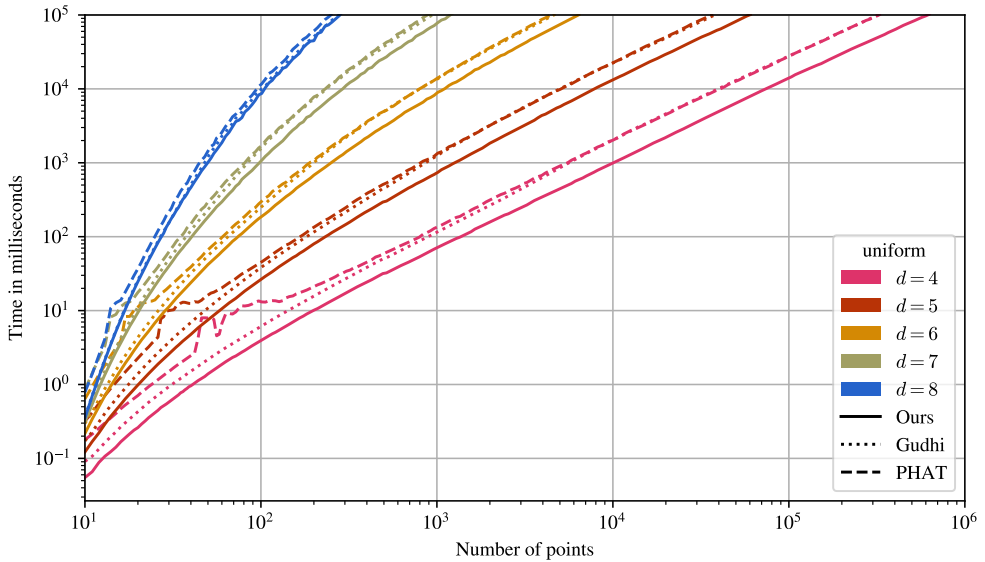


Fig. 10 Running time for computing the Delaunay–Rips persistence diagram of a uniformly distributed point cloud in \mathbb{R}^d , for varying $4 \leq d \leq 8$. We compare our approach with Gudhi [53] and PHAT [52].

Dimension d	3	4	5	6	7	8	9
Average overall timing ratio	0.29	0.50	0.58	0.63	0.64	0.76	1.44
Average PH timing ratio	0.20	0.33	0.39	0.44	0.55	0.73	1.46
Average memory ratio	0.35	0.26	0.19	0.19	0.20	0.19	0.24

Table 1 Average running time and memory consumption ratios of our method compared to PHAT, by dimension. The PH timing is obtained by removing the time required to compute the Delaunay complex.

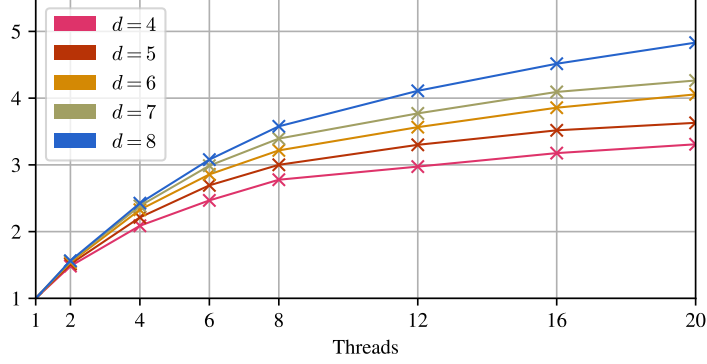


Fig. 11 Speedup of our method (excluding the Delaunay computation step) according to the number of threads. Computed for uniformly distributed point sets (200000 points for $d = 4$, 20000 points for $d = 5$, 2000 points for $d = 6$, 600 points for $d = 7$, 200 points for $d = 8$). Note that the CPU used for this experiment had a heterogeneous architecture with 8 fast cores (5.3 GHz) and 12 slower cores (3.8 GHz).

there is a single-thread bottleneck in the recovery of d -simplices in the Delaunay complex (to which CGAL’s implementation does not provide random-access). In our settings, this speedup reached around 3 for 8 threads and around 4 for 20 threads. In addition, it tends to increase with the ambient dimension.

Number of simplices

Tab. 2 gives the number of non-zero persistence pairs, the number of k -cells, and the size of MSA^k , US^k and DEL^k , with various ambient dimensions d and point cloud distributions (uniformly in $[-1, 1]^d$ or next to the sphere \mathbb{S}^{d-1}). Examining the quantities $1 - |\text{cells}^k|/|\text{MSA}^k|$ (where $|\text{cells}^k|$ is the number of k -cells delimited by $\text{US}^k \cup \text{NM}^k$ within MSA^{k+1}) gives an idea of the proportion of column reductions that are avoided by considering the k -cells instead of individual MSA^k simplices, which allows for a faster reduction step. In particular, one can observe that $|\text{cells}^k|/|\text{MSA}^k|$ tend to increase with the ambient dimension d , explaining the decreasing speedup noticed in Tab. 1, until it becomes unprofitable to compute these cells compared to the benefits it provides.

Persistent generators

We also implemented, for $d = 3$, the recovery of PH^1 and PH^2 persistent generators, which permits to have topological representations of each significant handle and cavity in the point cloud. More precisely, the generator associated with a persistent pair (σ, τ) is the set of simplices in the column of the cell associated with τ after the reduction. The 1-generators (resp. 2-generators) consist of $\text{UG} \cup \text{NM}^1$ edges (resp. US^2 triangles) only. While these generators are topologically correct, note that nothing encourages them to have a good geometric quality. Fig. 12 shows PH^1 generators computed for points sampled on surface in \mathbb{R}^3 of genus 0, 1, and 3.

d	n	distrib.	k	$ \text{PH}^{k-1} $	$ \text{cells}^k $	$ \text{MSA}^k $	$ \text{US}^k $	$ \text{DEL}^k $	$\frac{ \text{cells}^k }{ \text{MSA}^k }$	$\frac{ \text{cells}^k }{ \text{DEL}^k }$
3	10000	uniform	1	9999	9999	9999	15609	76690	1.00	0.13
			2	5610	24783	66691	71315	133258	0.37	0.19
			3	2938	4624	/	/	66567	/	0.07
	1000	sphere	1	9999	9999	9999	12827	64045	1.00	0.16
			2	2828	18570	54046	54379	103762	0.34	0.18
			3	174	333	/	/	49716	/	0.01
4	1000	uniform	1	999	999	999	1713	16109	1.00	0.06
			2	714	5517	15110	16942	54026	0.37	0.10
			3	433	15218	38916	40455	64547	0.39	0.24
			4	297	1539	/	/	25631	/	0.06
	100	sphere	1	999	999	999	1539	11549	1.00	0.09
			2	540	3872	10550	11386	32686	0.37	0.12
			3	277	8305	22136	22592	34720	0.38	0.24
			4	26	456	/	/	12584	/	0.04
5	100	uniform	1	99	99	99	161	1922	1.00	0.05
			2	62	617	1823	2942	9812	0.34	0.06
			3	26	3793	7989	8513	19935	0.47	0.19
			4	21	4477	11946	12229	17652	0.37	0.25
			5	10	283	/	/	5706	/	0.05
	10	sphere	1	99	99	99	163	1561	1.00	0.06
			2	64	523	1462	2209	6837	0.36	0.08
			3	42	2688	5375	5747	12441	0.50	0.22
			4	37	2801	7066	7209	10121	0.40	0.28
			5	4	143	/	/	3055	/	0.05

Table 2 Number of non-zero persistence pairs and size of the different constructions for various ambient dimensions and point cloud distributions. $|\text{PH}^k|$ denotes the number of non-zero k -dimensional persistence pairs. $|\text{cells}^k|$ denotes the number of k -cells delimited by $\text{US}^k \cup \text{NM}^k$ within MSA^{k+1} .

Conclusion

In this work, we performed a theoretical and empirical study of the behavior of persistence diagrams for the Delaunay–Rips filtration of point clouds. In particular, we studied the stability of the associated persistence diagrams in terms of bottleneck distance, and how they approximate the more common Rips persistence diagrams. Then, we proposed a fast and memory-efficient algorithm that computes these Delaunay–Rips persistence diagrams of low-dimensional point clouds, leveraging the specific structure of the filtration. This algorithm, supported by our theoretical and experimental study, makes the Delaunay–Rips filtration a relevant candidate in practice for the fast computation of persistent homology of point clouds in low-dimension. In particular, it may serve as a way to devise topological losses for machine learning algorithms involving three-dimensional point clouds or low-dimensional latent spaces. For future work, we will consider the generalization of certain of our results to other flag filtrations, enabling hopefully faster computations by discarding efficiently non relevant simplices or efficiently merging simplices into fewer, larger cells.

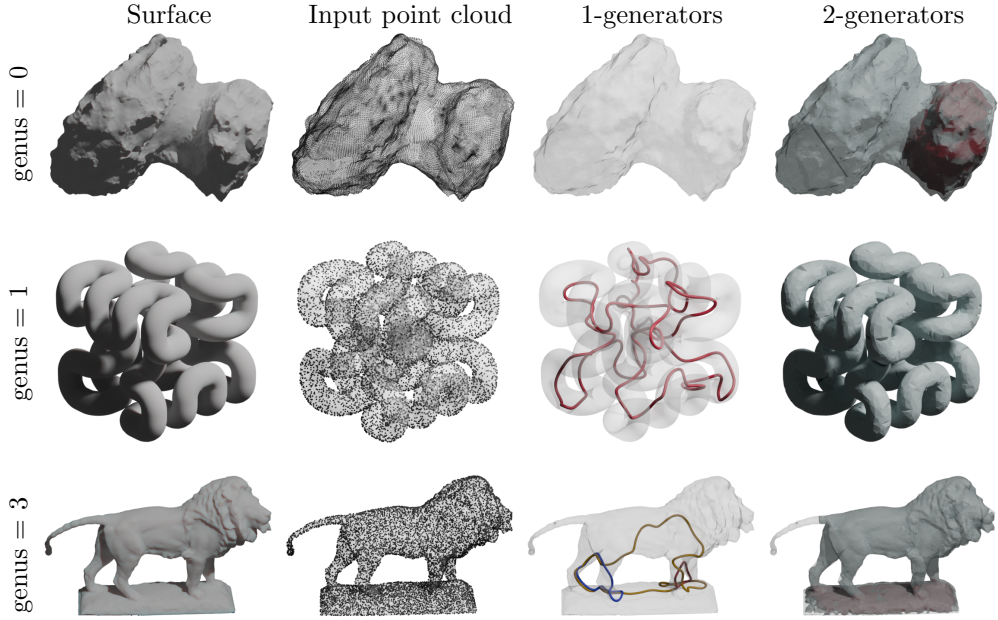


Fig. 12 1- and 2-dimensional persistent generators for point clouds sampled on surfaces of genus 0 (comet, top line), genus 1 (Hilbert curve, middle line), and genus 3 (lion statue, bottom line). Only persistent generators with significant persistence are shown. Only the largest connected component of each 1-generator was kept and was smoothed for readability. 1- and 2-generators can be interpreted respectively as the topological handles and topological cavities of the input point cloud.

Acknowledgments

This work is partially supported by the European Commission grant ERC-2019-COG “*TORI*” (ref. 863464, <https://erc-tori.github.io/>); and by ANR-23-PEIA-0004 (PDE-AI, <https://pde-ai.math.cnrs.fr/>).

References

- [1] Bauer, U.: Ripser: efficient computation of Vietoris–Rips persistence barcodes. *Journal of Applied and Computational Topology* (2021)
- [2] Pérez, J.B., Hauke, S., Lupo, U., Caorsi, M., Dassatti, A.: giotto-ph: a Python library for high-performance computation of persistent homology of Vietoris–Rips filtrations. *arXiv preprint arXiv:2107.05412* (2021)
- [3] Zhang, S., Xiao, M., Wang, H.: GPU-accelerated computation of Vietoris–Rips persistence barcodes. *arXiv preprint arXiv:2003.07989* (2020)
- [4] Edelsbrunner, H., Mücke, E.P.: Three-dimensional alpha shapes. *ACM Transactions On Graphics (TOG)* **13**(1), 43–72 (1994)

- [5] Bauer, U., Edelsbrunner, H.: The Morse theory of Čech and Delaunay complexes. *Transactions of the American Mathematical Society* **369**(5), 3741–3762 (2017)
- [6] Gabrielsson, R.B., Nelson, B.J., Dwaraknath, A., Skraba, P.: A topology layer for machine learning. In: International Conference on Artificial Intelligence and Statistics, pp. 1553–1563 (2020). PMLR
- [7] Mishra, A., Motta, F.C.: Stability and machine learning applications of persistent homology using the Delaunay–Rips complex. *Frontiers in Applied Mathematics and Statistics* **9**, 1179301 (2023)
- [8] Tauzin, G., Lupo, U., Tunstall, L., Pérez, J.B., Caorsi, M., Medina-Mardones, A.M., Dassatti, A., Hess, K.: giotto-tda: A topological data analysis toolkit for machine learning and data exploration. *Journal of Machine Learning Research* **22**(39), 1–6 (2021)
- [9] Morozov, D., Nigmetov, A.: Towards lockfree persistent homology. In: Proceedings of the 32nd ACM Symposium on Parallelism in Algorithms and Architectures, pp. 555–557 (2020)
- [10] Sheehy, D.R.: Linear-size approximations to the Vietoris–Rips filtration. In: Proceedings of the Twenty-eighth Annual Symposium on Computational Geometry, pp. 239–248 (2012)
- [11] Kerber, M., Sharathkumar, R.: Approximate čech complex in low and high dimensions. In: International Symposium on Algorithms and Computation, pp. 666–676 (2013). Springer
- [12] Cavanna, N.J., Jahanseir, M., Sheehy, D.R.: A geometric perspective on sparse filtrations. arXiv preprint arXiv:1506.03797 (2015)
- [13] Boissonnat, J.-D., Pritam, S.: Edge collapse and persistence of flag complexes. In: 36th International Symposium on Computational Geometry (SoCG 2020), pp. 19–1 (2020). Schloss Dagstuhl–Leibniz-Zentrum für Informatik
- [14] Glisse, M., Pritam, S.: Swap, shift and trim to edge collapse a filtration. arXiv preprint arXiv:2203.07022 (2022)
- [15] De Silva, V., Carlsson, G.: Topological estimation using witness complexes. In: Proceedings of the First Eurographics Conference on Point-Based Graphics, pp. 157–166 (2004)
- [16] Graf, F., Pellizzoni, P., Uray, M., Huber, S., Kwitt, R.: The flood complex: Large-scale persistent homology on millions of points. arXiv preprint arXiv:2509.22432 (2025)
- [17] Zhou, C., Dong, Z., Lin, H.: Learning persistent homology of 3D point clouds.

- [18] Surrel, T., Hensel, F., Carrière, M., Lacombe, T., Ike, Y., Kurihara, H., Glisse, M., Chazal, F.: RipsNet: a general architecture for fast and robust estimation of the persistent homology of point clouds. In: Topological, Algebraic and Geometric Learning Workshops 2022, pp. 96–106 (2022). PMLR
- [19] Wang, Y., Sun, Y., Liu, Z., Sarma, S.E., Bronstein, M.M., Solomon, J.M.: Dynamic graph CNN for learning on point clouds. ACM Transactions on Graphics (tog) **38**(5), 1–12 (2019)
- [20] Zaheer, M., Kottur, S., Ravanbakhsh, S., Poczos, B., Salakhutdinov, R.R., Smola, A.J.: Deep sets. Advances in neural information processing systems **30** (2017)
- [21] Koyama, M.A., Memoli, F., Robins, V., Turner, K.: Faster computation of degree-1 persistent homology using the reduced Vietoris–Rips filtration. arXiv preprint arXiv:2307.16333 (2023)
- [22] Clémot, M., Digne, J., Tierny, J.: Topological Autoencoders++: Fast and Accurate Cycle-Aware Dimensionality Reduction (2025)
- [23] Corbet, R., Kerber, M., Lesnick, M., Osang, G.: Computing the multicover bifiltration. Discrete & Computational Geometry **70**(2), 376–405 (2023)
- [24] Blaser, N., Brun, M., Gardaa, O.H., Salbu, L.M.: Core bifiltration. arXiv preprint arXiv:2405.01214 (2024)
- [25] Alonso, Á.J., Kerber, M., Lam, T., Lesnick, M.: Delaunay bifiltrations of functions on point clouds. In: Proceedings of the 2024 Annual ACM-SIAM Symposium on Discrete Algorithms (SODA), pp. 4872–4891 (2024). SIAM
- [26] Amenta, N., Attali, D., Devillers, O.: Complexity of Delaunay triangulation for points on lower-dimensional polyhedra. In: ACM-SIAM Symposium on Discrete Algorithms, pp. 1106–1113 (2007)
- [27] Boissonnat, J.-D., Devillers, O., Hornus, S.: Incremental construction of the Delaunay triangulation and the Delaunay graph in medium dimension. In: Proceedings of the Twenty-fifth Annual Symposium on Computational Geometry, pp. 208–216 (2009)
- [28] Devillers, O., Hornus, S., Jamin, C.: dD Triangulations. CGAL Editorial Board (2024)
- [29] Edelsbrunner, H., Harer, J.L.: Computational topology: an introduction. AMS (2010)
- [30] Zomorodian, A.: Computational topology. In: Algorithms and Theory of Computation Handbook: Special Topics and Techniques, 2nd edn. (2010)

- [31] Chazal, F., De Silva, V., Glisse, M., Oudot, S.: The structure and stability of persistence modules. Springer (2016)
- [32] Chazal, F., Cohen-Steiner, D., Glisse, M., Guibas, L.J., Oudot, S.Y.: Proximity of persistence modules and their diagrams. In: Proceedings of the Twenty-fifth Annual Symposium on Computational Geometry, pp. 237–246 (2009)
- [33] Bauer, U., Kerber, M., Roll, F., Rolle, A.: A unified view on the functorial nerve theorem and its variations. *Expositiones Mathematicae* **41**(4), 125503 (2023)
- [34] Jung, H.: Über die kleinste Kugel, die eine räumliche Figur einschliesst. *Journal für die reine und angewandte Mathematik (Crelles Journal)* **1901**(123), 241–257 (1901)
- [35] Chazal, F., Cohen-Steiner, D., Guibas, L.J., Mémoli, F., Oudot, S.Y.: Gromov–Hausdorff stable signatures for shapes using persistence. In: Computer Graphics Forum, vol. 28, pp. 1393–1403 (2009). Wiley Online Library
- [36] Chazal, F., De Silva, V., Oudot, S.: Persistence stability for geometric complexes. *Geometriae Dedicata* **173**(1), 193–214 (2014)
- [37] Skraba, P., Turner, K.: Wasserstein stability for persistence diagrams. arXiv preprint arXiv:2006.16824 (2020)
- [38] Kalai, G.: Enumeration of \mathbb{Q} -acyclic simplicial complexes. *Israel Journal of Mathematics* **45**(4), 337–351 (1983)
- [39] Skraba, P., Thoppe, G., Yogeshwaran, D.: Randomly weighted d –complexes: Minimal spanning acycles and persistence diagrams. arXiv preprint arXiv:1701.00239 (2017)
- [40] Skraba, P., Yogeshwaran, D.: Central limit theorem for euclidean minimal spanning acycles. *Journal of Topology and Analysis* **17**(04), 931–967 (2025)
- [41] Cormen, T., Leiserson, C.E., Rivest, R.L., Stein, C.: Introduction to Algorithms. MIT Press (2009)
- [42] Toussaint, G.T.: The relative neighbourhood graph of a finite planar set. *Pattern recognition* (1980)
- [43] Supowit, K.J.: The relative neighborhood graph, with an application to minimum spanning trees. *JACM* (1983)
- [44] Jaromczyk, J.W., Kowaluk, M.: A note on relative neighborhood graphs. In: Proceedings of the Third Annual Symposium on Computational Geometry (1987)
- [45] Lingas, A.: A linear-time construction of the relative neighborhood graph from the Delaunay triangulation. *Computational Geometry* (1994)

- [46] Urquhart, R.: Algorithms for computation of relative neighbourhood graph. *Electronics Letters* (1980)
- [47] Hatcher, A.: Algebraic topology. Cambridge University Press (2002)
- [48] Jamin, C., Pion, S., Teillaud, M.: 3D Triangulations. CGAL Editorial Board (2024)
- [49] Anderson, R.J., Woll, H.: Wait-free parallel algorithms for the union-find problem. In: Proceedings of the Twenty-third Annual ACM Symposium on Theory of Computing, pp. 370–380 (1991)
- [50] Guillou, P., Vidal, J., Tierny, J.: Discrete morse sandwich: Fast computation of persistence diagrams for scalar data – an algorithm and a benchmark. *IEEE Transactions on Visualization and Computer Graphics* **30**(4), 1897–1915 (2023)
- [51] Fabri, A., Pion, S.: CGAL: the Computational Geometry Algorithms Library. In: Proceedings of the 17th ACM SIGSPATIAL International Conference on Advances in Geographic Information Systems (2009)
- [52] Bauer, U., Kerber, M., Reininghaus, J., Wagner, H.: PHAT – Persistent homology algorithms toolbox. *Journal of symbolic computation* (2017)
- [53] Maria, C., Boissonnat, J.-D., Glisse, M., Yvinec, M.: The Gudhi library: Simplicial complexes and persistent homology. In: ICMS (2014)
- [54] Bauer, U., Kerber, M., Reininghaus, J., Wagner, H., Skraba, P.: PHAT (Persistent Homology Algorithm Toolbox), v1.4.0. GitHub. https://github.com/blazs/phat/blob/master/addons/alpha_3.cpp (2015)
- [55] Rouvreau, V.: Alpha complex. GUDHI Editorial Board. https://gudhi.inria.fr/doc/3.11.0/group_alpha_complex.html (2025)
- [56] Maria, C.: Persistent Cohomology. GUDHI Editorial Board. https://gudhi.inria.fr/doc/3.11.0/group_persistent_cohomology.html (2025)
- [57] Virtanen, P., Gommers, R., Oliphant, T.E., Haberland, M., Reddy, T., Cournapeau, D., Burovski, E., Peterson, P., Weckesser, W., Bright, J., *et al.*: SciPy 1.0: fundamental algorithms for scientific computing in Python. *Nature methods* **17**(3), 261–272 (2020)